Quantifying Aspect-Dependent Snowpack Response to High-Elevation Wildfire in the Southern Rocky Mountains

W. Reis[1,2], D. McGrath[1], K. Elder[3], S. Kampf[4] and D. Rey[5]

[1]Colorado State University, Department of Geosciences, Fort Collins, CO, USA

[2]Cold Regions Research and Engineering Laboratory, Engineering Research and Development Center, Hanover, NH, USA

[3]United States Forest Service, Rocky Mountain Research Station, Fort Collins, CO, USA

[4]Colorado State University, Department of Ecosystem Science and Sustainability, Fort Collins, CO, USA

[5] United States Geological Survey, Observing Systems Division, Denver, CO, USA

Corresponding authors: Wyatt Reis (wyatt.reis@colostate.edu), Daniel McGrath (daniel.mcgrath@colostate.edu)

Key Points:

- The burned south site reached peak snow water equivalent 22 days earlier than all other sites, which occurred simultaneously.
- Burned site melt rates were similar between aspect but exceeded unburned sites by 71–94%. Burned sites became snow free 7–11 days earlier.
- Burned site net shortwave increased from 56–137% greater during ablation, and net longwave was consistently lower, than the unburned site.

Abstract

Increasing wildfire frequency and severity in high-elevation seasonal snow zones presents a considerable water resource management challenge across the western U.S. Wildfires can affect snowpack accumulation and melt patterns, altering the quantity and timing of runoff. While prior research has shown that wildfire generally increases snow melt rates and advances snow disappearance dates, uncertainties remain regarding variations across complex terrain and the energy balance between burned and unburned areas. Utilizing multiple paired in-situ data sources within the 2020 Cameron Peak burn area during the 2021–2022 winter, we found no significant difference in peak snow water equivalent (SWE) magnitude between burned and unburned areas. However, the burned south aspect reached peak SWE 22 days earlier than burned north. During the ablation period, burned south melt rates were 71% greater than unburned south melt rates, whereas burned north melt rates were 94% greater than unburned north aspects. Snow disappeared 7 to 11 days earlier in burned areas than unburned areas. Net energy differences at the burned and unburned AWS sites were seasonally variable, with the burned area losing more energy during the winter but gaining significantly more energy during the spring. Net shortwave radiation was 56% greater at the burned area during the winter and 137% greater during the spring driving a ~60% greater cumulative net energy at the burned site during May. These findings emphasize the need for post-wildfire water resource planning that accounts for aspect-dependent differences in energy and mass balance to accurately predict snowpack storage and runoff timing.

Plain Language Summary

Wildfires are occurring more often at high-elevations, complicating efforts to accurately predict when snowmelt runoff will occur and the amount of water that will melt from the snowpack. Following wildfire, the amount of snow available for melt varies based on the study location, but generally snow melt occurs earlier in the year and at a faster rate. However, in complex, mountainous terrain, it is not well understood how the magnitude of these changes may differ between neighboring slopes. During the 2021–22 winter in the Cameron Peak burn area (2020) in Colorado, we found that in a high-elevation snowpack there was no difference in the amount of water accumulated in the snowpack between areas that were burned by the fire and areas that were not. But in areas that burned, the amount of water in the snowpack reached its greatest amount 22 days earlier than the areas that did not burn. The snowpack melted faster on both south and north facing slopes in the burned area compared to the unburned area, causing the burned areas to be snow free 7 to 11 days earlier. These results highlight the need to account complex terrain in water resource planning.

1 Introduction

Across North America, 60% of seasonal snow accumulates in mountainous regions, causing distinct seasonal hydrologic cycles in snow-dominated watersheds (Bales et al., 2006; Wrzesien et al., 2018). For these basins, 60–80% of spring and summer streamflow is derived from liquid water stored in seasonal snowpacks (Li et al., 2017). Consequently, quantifying seasonal snow accumulation and ablation dynamics can help inform the management of downstream water supplies, hydropower generation, and agricultural production (Barnett et al., 2005; Viviroli et al., 2007; Li et al., 2017; Sturm et al., 2017). However, over the last century, 1 April SWE has declined by ~20% across the western U.S. (Mote et al., 2005, 2018), and in the last 50 years melt has initiated 1–3 weeks earlier (Cayan et al., 2001; McCabe and Clark, 2005; Clow, 2010; Hall et al., 2015; Dudley et al., 2017; Wagner et al., 2021), resulting in reduced melt rates, increased evapotranspiration, and reduced runoff generation (Barnhart et al., 2016; Musselman et al., 2017). Additionally, the hydrology within snow-dominated watersheds is bifurcating based on elevation with the lowest elevations moving toward dramatically declined peak SWE (14–45%), while peak SWE at high elevations is predicted to remain unchanged (Marshall et al., 2019; Hammond et al., 2023).

The changing timing and increased proportion of rain and earlier snowmelt/spring runoff within these snow-dominated watersheds reduces water storage and soil moisture, increasing the potential for wildfire activity during subsequent summers (O'Leary et al., 2016; Westerling, 2016; Hale et al., 2023; Hammond et al., 2023). Additionally, the increased aridity of the western U.S., along with a history of fire suppression, has led to a rapid growth in wildfire burn area, greater fire severity, and higher median elevation of wildfires over the last half-century, with an additional pronounced increase since the early 2000s (Westerling et al., 2006; Alizadeh et al., 2021; Iglesias et al., 2022; Shi and Touge, 2023). Between 1984–2017, western U.S. forests above 2500 m experienced a 270% increase in wildfire activity, with the median burned elevation increasing by 250 m (Alizadeh et al., 2021). Model projections indicate a 63–107% increase in mean annual wildfire burn area by the end of the century (Westerling et al., 2011; Mueller et al., 2020; Alizadeh et al., 2021). The expansion of wildfire into high-elevation forests has impacted seasonal snow zones greatly, with 70% of western U.S. ecoregions experiencing a significant increase in burned area within the late season snow zone (Kampf et al., 2022).

High-elevation forests regulate the accumulation and melt of seasonal snowpacks by altering wind speed, precipitation, and energy fluxes (Williams et al., 1972; Dozier, 1980; Troendle and King, 1985; Elder et al., 1989, 1991; Liston et al., 2007; Painter et al., 2007; Trujillo et al., 2007, 2009; Musselman et al., 2008; Biederman et al., 2014; Roth and Nolin, 2017). Thus, disturbances by wildfire have the potential to significantly alter the mass and energy balances of snow-dominated watersheds. The four primary alterations following wildfire include: (i) a reduction in canopy snowfall interception (Harpold et al., 2014; McGrath et al., 2023) and (ii) an increase in shortwave radiation reaching the snow surface (Burles and Boon, 2011), both due to canopy loss, (iii) a lower snow surface albedo from the accumulation of soot/burned debris (Gleason et al., 2013; Gleason and Nolin, 2016; Uecker et al., 2020), and (iv) increases in turbulent fluxes because of higher wind speeds due to the more open forest structure (Boon, 2009; Molotch et al., 2009). In most seasonal snow burned areas, these competing changes to the mass and energy balances decrease peak SWE while increasing melt rates, (Loiselle et al., 2020; Maina and Siirila-Woodburn, 2020; Smoot and Gleason, 2021; Giovando

and Niemann, 2022) yet the impact varies between ecoregions, as well as across snow zones (e.g. early vs late; Giovando and Niemann, 2022; Kampf et al., 2022). Further, the loss of canopy due to wildfire mimics forest harvest impacts by reducing summertime evapotranspiration, increasing soil moisture recharge, and ultimately increasing runoff (Troendle and King, 1985).

While a consensus is emerging on the primary impacts of wildfire on snow, prior work has not thoroughly evaluated how these impacts might vary across the complex topography that characterizes high-elevation mountain environments in the western U.S. Furthermore, few studies have assessed how the changes in forest structure post-fire influence all components of the snowpack energy balance. Our work addresses these two key knowledge gaps:

(i) How do snowpacks vary across complex terrain following wildfire? Aspect exerts a strong control on seasonal snowpacks (e.g., Elder et al., 1991; Anderson et al., 2014), but most previous post-wildfire snowpack studies have not focused on identifying the way changes in quantity and date of peak SWE, and melt rates are modulated by complex terrain in wildfire burned areas. In the limited number of studies that incorporated differences in aspect, the greatest declines in snow depth and advances in snow disappearance dates occurred on south-facing slopes (Maxwell et al., 2019; Moeser et al., 2020).

(ii) How does wildfire affect the energy balance (shortwave radiation, longwave radiation, and turbulent fluxes) of the snowpack? Prior studies have consistently attributed the observed increases in melt rates post-fire to an increase in shortwave radiation reaching the snow surface and a decrease in snow surface albedo (Burles and Boon, 2011; Gleason et al., 2013; Harpold et al., 2014). However, the other components (longwave radiation, turbulent fluxes) of the energy balance have not been systematically assessed post-fire.

We address these knowledge gaps using multiple sources of data including bi-weekly manual snowpack measurements and two continuous automatic weather stations paired across aspect and burn condition in the Cameron Peak burn scar, Colorado, during the 2021–22 winter.

2 Study Site

We established a study area at an elevation of ~3050 m within the sub-alpine zone of the Cache la Poudre watershed approximately 5 km north of Cameron Pass in northcentral Colorado (Figure 1a and Figure 1b). The 2 km^2 study area is situated in a mixed forest of subalpine fir (Abies lasiocarpa), Douglas fir (Pseudotsuga menziesii), and Engelmann spruce (Picea engelmannii) and is within the persistent seasonal snow zone (SSZ; Moore et al., 2015). The study area sampled the range of burn severities present in the burned SSZ, but given the burn conditions in the study area, oversampled high-burn severities and under sampled low- to moderate burn severities (Figure 1f). Similarly, the study site spanned the range of northness values (defined below) present within the burned SSZ (Figure 1g).

In the study area, we installed an automated weather station (AWS) in January 2021 in a high burn severity location (Burned – AWS; Figure 1). In November 2021, we installed an additional AWS in a ~5 m by 5 m forest gap representative of unburned forests in the area (Unburned – AWS). Additionally, we measured snow depth at an under-canopy location (Unburned – UC) with an automated sonic snow depth sensor. These three sites have comparable

141 southeast aspects with northness values ranging between –0.12–0.02 and slope angles between
142 2.8–6.3° (Table 1). In November 2021, we established three additional sites to measure snow
143 depth with time-lapse cameras and snow depth poles on sloped terrain (Burned – North, Burned
144 – South, Unburned – North: Table 1; Figure 1b and Figure 1c). Four ~500 m snow depth
145 transects were also established and covered a range of aspects in burned and unburned locations
146 (Figure 1b and Figure 1c).

147 The Joe Wright SNOTEL (ID 551) is located about 80 m higher and 3.5 km southwest of
148 the main study area. The SNOTEL measured average winter SWE accumulation, with a
149 maximum SWE of 632 mm on 10 May compared to the 1991–2020 median of 622 mm on 6
150 May. Snow disappearance at the site occurred on 15 June 2022, just two days earlier than the 17
151 June 30-year median snow disappearance date (SDD).

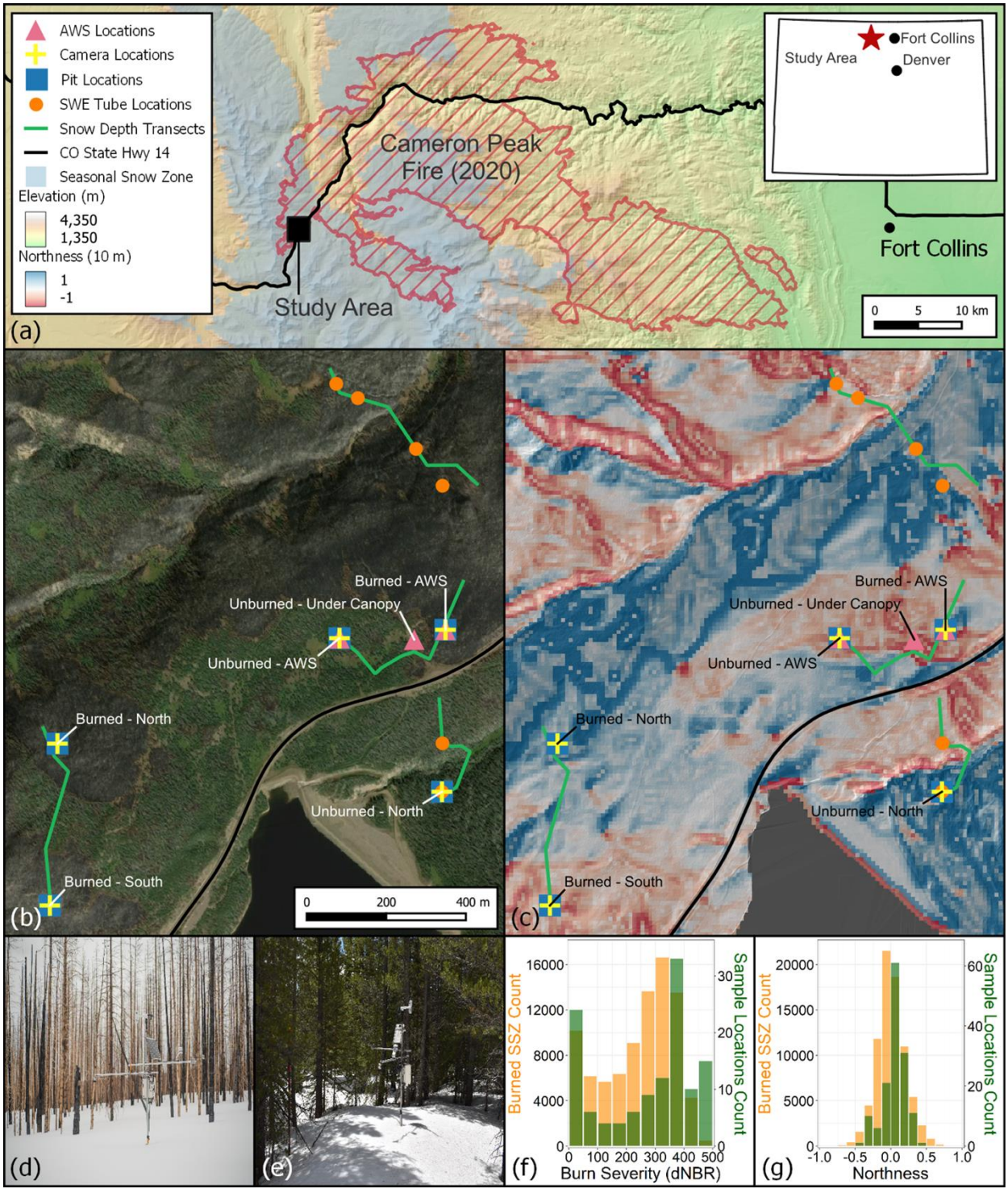

Figure 1. (a) Study area location within 2020 Cameron Peak wildfire burn area and the persistent seasonal snow zone (SSZ; Moore et al., 2015). (b) Maxar optical imagery of the study with study site locations overlaid. (c) Northness (10 m resolution) for the study area. (d) Burned-area AWS. (e) Unburned-area AWS. (f) Histogram of binned differenced normalized burn ratio (dNBR) within the SSZ impacted by the Cameron Peak fire (orange) and the repeat snow depth transect locations (green). On the dNBR scale, moderate–low severity burn values range from 270–439

and moderate–high burn severity values are between 440–659. (g) Histogram of northness values within the burned SSZ (orange) and the sampled locations (green). Northness values greater than 0 are north-facing, while values less than 0 are south-facing.

Table 1. Study site locations, difference normalized burn ratios (dNBR), elevations, and topographic characteristics.

Site Name	Coordinates (degrees)	dNBR (unitless)	Elevation (m a.s.l.)	Aspect (deg)	Slope (deg)	Northness (–1 to 1)
Burned –AWS	(40.564, –105.867)	373	3009	65	2	0.02
Burned – North (Camera)	(40.561, –105.879)	355	3095	40	13	0.16
Burned – South (Camera)	(40.558, –105.879)	464	3102	220	20	–0.26
Unburned – AWS	(40.563, –105.870)	–	3019	175	7	–0.12
Unburned – North (Camera)	(40.560, –105.867)	–	2991	15	24	0.39
Unburned – Under-Canopy (UC)	(40.564, –105.868)	–	3010	170	5	–0.08

3 Materials and Methods

3.1 Automated Weather Stations

The burned and unburned AWS measure air temperature and relative humidity *(Campbell Scientific HydroVUE5)*, snow depth *(Campbell Scientific SR50A)*, snow/soil temperature and relative permittivity *(Campbell Scientific SoilVUE10; unburned, 1 m length; burned, 0.5 m length)*, wind speed and direction *(RM Young 05103 Wind Monitor)*, barometric pressure *(Campbell Scientific CS100; burned only)*, and four-component net radiation *(Apogee SN500SS)*. The AWS sites were programmed to collect data every minute and logged the fifteen minute and hourly mean values. The UC site was instrumented with a standalone sonic snow depth sensor *(A2 Photonic Sensors SPICE)*.

We also measured snow depth at the two AWS sites and at three additional snow depth sites using time-lapse cameras (*Wingscapes TimelapseCam Pro*) and snow depth poles with 10 cm gradation (Figure 1b). At the time-lapse sites, we installed three snow depth poles at locations without a weather station and one pole at the AWS sites. We programmed the time-lapse cameras to capture an hourly photo between 0700 and 1900. Using the photos from noon (1200) or the next interpretable photo, we manually recorded daily snow depths with 5 cm precision and calculated the average daily snow depth for the site.

3.2 Manual Snowpack Measurements

From 14 November – 13 June, we collected snow pit and snow depth transect data approximately every other week. The snow pit observations were co-located with the two AWS and three snow depth camera sites and included vertical profiles (10 cm increments) of snow density, dielectric permittivity, and temperature, as well as snow stratigraphy, and grain size profiles by layer. Pits were dug with the measurement wall facing north to minimize ambient weather effects on the measurements. We dug the snow pits in the same general location each time but shifted them ~1 m behind the previous pit wall and backfilled the pits following data collection to minimize the influence of the previous pit face.

Snow depths along each of the four transects were collected during the same week as snow pit observations. Snow depths were measured using a 3 m Snowmetrics probe with 1 cm gradations and taken in a 1 m five-point "star" pattern (Harpold et al., 2014), every ~15 m along the transects. Each measurement was geolocated using a Juniper Systems Geode GNSS receiver (<30 cm horizontal accuracy), allowing us to collect snow depth in repeat locations throughout the winter. Mean snow depth for each location was calculated using the five snow depths and slope, aspect, and burn condition was assigned to each location based on the post-fire 2021 lidar-derived DEM (0.7 m resolution) and the post-fire difference Normalized Burn Ratio (dNBR) burn severity map (Woodward and Vorster, personal communication). We subsequently refer to these distributed measurements as "probe-derived." While completing snow depth transects, bulk snowpack density measurements were also collected using a Snow-Hydro SWE Coring Tube at six locations (Figure 1b and Figure 1c).

3.3 Snow Surface Albedo Measurements

To reduce noise in the unburned AWS shortwave radiation data, we calculated daily albedo from median hourly values between 1000–1400 each day and applied a 7-day median smoothing function at both weather stations.

Spectral albedo observations were also collected in the burned forest and an open unburned meadow near the burned and unburned AWS sites under clear-sky conditions on 15 May. We used a Malvern Panalytical/Analytical Spectral Devices (ASD) FieldSpec 4 Standard-Res spectroradiometer (3 nm VNIR, 10 nm SWIR resolution) at six locations evenly split between the burned and the unburned areas. At each of the locations, five upwelling and five downwelling measurements were taken within 2 hours of solar noon using the ASD remote cosine reflector on an outstretched 60 cm metal arm to the south of a tripod. Each of the five manually triggered observations collected five automated measurements. Albedo was calculated as the ratio of the mean upwelling and downwelling radiation measurements and is presented here as the mean albedo at the burned and unburned sites.

3.4 Snow Water Equivalent Calculations

Using the density profiles from each snow pit, we calculated the bulk snow density. Combining the bulk pit densities with density from the six SWE tube locations, we calculated the mean density for each aspect and burn condition. Bulk snowpack density was then linearly interpolated between sampling dates to attain an estimate of daily bulk density. Mean daily SWE was calculated for each aspect and burn condition by multiplying the daily bulk density by the probe depth measurements. The mean SWE was then calculated for each aspect and burn

condition by grouping the sites by aspect and burn condition. Mean continuous SWE measurements were calculated for each burn condition and aspect using the continuous snow depth measurements from the time-lapse cameras and sonic snow depth sensors. To calculate the SWE, we applied the linearly interpolated snow densities by burn condition and site aspect. These continuous sites will be referred to as "continuous SWE."

3.5 Terrain and Cold Content Analysis

As a measure of terrain aspect, we calculated northness (Molotch et al., 2005),

$$Northness = \cos(aspect\ (°)) \times \sin(slope\ angle\ (°)). \#(1)$$

To determine the slope angle and topographic aspect at each point, we used a USGS LiDAR-derived DEM with a 0.7 m spatial resolution. While the 0.7 m resolution DEM was used in all analysis, we down-sampled the northness raster to 10 m resolution for clarity in Figure 1.

Cold content is a measure of the snowpack energy deficit, which depends on the snowpack's temperature and mass. This deficit must be overcome before snowmelt runoff can occur. We calculated cold content for each study site as:

$$CC = c_i \rho_s d_s (T_S - T_m), \#(2)$$

where CC is the snowpack cold content (MJ m^{-2}), c_i is the specific heat of ice (2.1x 10^{-3} MJ kg^{-1} $°C^{-1}$), ρ_s is the density of snow (kg m^{-3}), d_s is snow depth (m), T_S is the depth weighted snowpack temperature (°C), and T_m is the melting temperature of snow (0 °C). To be more representative of the study area, we calculated cold content using the median probe snow depth in each burn condition (burned/unburned) and aspect (north/south) instead of using the snow pit depth.

3.6 Snowpack Energy Balance Analysis

Using the AWS station observations at both the burned and unburned AWS sites, we calculated the total energy using a simple one-dimensional (vertical) model:

$$Q = K + L + H + L_v E + R + G \#(3)$$

where Q is the total energy available, K is the net shortwave radiation, L is the net longwave radiation, H is the sensible heat flux, and $L_v E$ is the latent heat flux. The energy inputs from rainfall (R) and the ground heat flux (G) were not included since no rain was observed during the observational period, and the ground heat flux is assumed to be negligible (Boon, 2009). All terms have units of W m^{-2}.

3.6.1 Shortwave and Longwave Radiation

For each site, we calculated K and L from the mean hourly observations using:

$$K = K_{in} - K_{out} \#(4)$$

and,

$$L = L_{in} - L_{out} \#(5)$$

where K_{in} and L_{in} are the incoming radiation components (W m^{-2}), while K_{out} and L_{out} are the outgoing radiation components (W m^{-2}). Hours with incoming shortwave radiation values less than outgoing shortwave radiation were removed since these are not physically realistic and are likely due to snow covering the upward-looking sensor. As a result, for days with less than six hours of recorded shortwave data, we did not assess the energy balance at that site (n=17; Figure S1).

3.6.2 Turbulent Energy Flux Modeling

We measured wind speed at two locations, the burned AWS and the unburned AWS. Wind speed and air temperature were measured 3 m above the ground surface at the burned and unburned sites. We logarithmically extrapolated wind speeds and linearly extrapolated air temperatures to the height of the snow surface to calculate the sensible and latent heat fluxes (Boon, 2009; Mandal et al., 2022).

For each of the sites, hourly H and L_vE were calculated as a function of the temperature, vapor pressure, and wind speed gradients above the surface of the of the snow,

$$H = \rho_a C_p D_H (T_a - T_{ss}), \#(6)$$

$$L_vE = \rho_a \lambda_v D_E \frac{0.622}{10P_a}(e_a - e_s), \#(7)$$

where ρ_a is the air density at the sites (kg m^{-3}),

$$\rho_a = \frac{0.34722 \times P_a}{T_a}, \#(8)$$

where P_a is the air pressure (mbar) at each site. Since air pressure was only recorded at the burned AWS and both sites are within 500 m of each other and at similar elevations, the burned AWS air pressure was used at both sites. The specific heat capacity of air (C_p) was set as 1005 J kg^{-1} K^{-1}. T_a is the air temperature (ºK) and the snow surface temperature (T_{ss}; ºK) was calculated using,

$$T_{ss} = \left(\frac{L_{out}}{\varepsilon_s \sigma}\right)^{\frac{1}{4}}, \#(9)$$

where the emissivity (ε_s) of the snow surface is assumed to be 0.97 (Hardy et al., 1997), and σ is the Stefan-Boltzmann constant (5.67×10^{-8} W m^{-2} K^{-4}).

The latent heat of vaporization (λ_v; MJ kg^{-1}) was given by,

$$\lambda_v = 2.501 - 0.002361(t_{ss}), \#(10)$$

where t_{ss} is the snow surface temperature in degrees Celsius.

Using Teten's formula (Murray, 1967), we calculated the saturation vapor pressure of the air ($e_{a_{sat}}$) and the snow surface ($e_{s_{sat}}$) in kPa,

$$e_{a_{sat}} \; or \; e_{s_{sat}} = \begin{cases} 6.11 \times exp\left(\frac{17.27 t_{a\ or\ ss}}{t_{a\ or\ ss} + 237.3}\right); \; t_{a\ or\ ss} > 0℃ \\ 6.11 \times exp\left(\frac{21.87 t_{a\ or\ ss}}{t_{a\ or\ ss} + 265.5}\right); \; t_{a\ or\ ss} \leq 0℃ \end{cases}, \#(11)$$

where $t_{a\ or\ ss}$ is either the air temperature (t_a) or snow surface temperature (t_{ss}) in degrees Celsius. We assumed the snow surface vapor pressure (e_s) was always saturated, giving $e_s = e_{s_{sat}}$, but to determine the air vapor pressure (e_a), we used,

$$e_a = \frac{RH}{100\%} \times e_{a_{sat}}, \#(12)$$

where RH is the hourly measured relative humidity (%) at each AWS site.

Finally, D_H and D_E are the bulk transfer coefficients of sensible and latent heat (m s^{-1}). Under neutral atmospheric conditions, D_H and D_E are assumed to be equivalent to each other and calculated as:

$$D_H = D_E = \frac{k^2 u}{\left[\ln\left(\frac{z_u}{z_0}\right)\right]^2}, \#(13)$$

where k is the von Karman constant (0.4) and z_0 is the roughness length (m). Due to a lack of field measurements, we assumed all roughness lengths to be 0.006 m following Boon (2009). The wind speed measurement height (z_u) is the time-varying height (m) above the snowpack surface at each site.

To account for the stability of the surface boundary layer and correct the turbulent fluxes under highly variable conditions we used the Richardson number (R_i; Brutsaert, 1982) :

$$R_i = g \frac{(T_a - T_{ss})\, z_u}{T_a u^2}, \#(14)$$

where g is gravitation acceleration (9.81 m s^{-2}), u is the hourly average wind speed (m s^{-1}) measured at each site. Due to substantial variability, potential hysteresis, and a wide-range in published values and approaches in the determination of the R_i critical number (Andreas, 2002), and a sizable portion of the R_i values falling below zero, turbulence was dampened when R_i was not between –0.4 and 0.3 (Andreas, 2002; Boon, 2009; Mandal et al., 2022). The turbulence was dampened for stable atmospheric conditions using,

$$D_{H_C} = D_{E_C} = \frac{D_H}{(1 + 10R_i)}. \#(15)$$

4 Results

Wildfire directly changes canopy and forest structure, thereby altering the snowpack energy balance. To provide insight as to how snowpacks change across complex terrain following wildfire, we use the periodic in-situ data to address differences in i) the quantity and date of peak SWE and ii) the melt rates and snow disappearance dates. Second, using the paired

304 burned and unburned AWS data, we assess iii) how components of the seasonal snowpack
305 energy balance vary between burned and unburned sites.

306 ## 4.1 Aspect Influence on Quantity and Timing of Peak SWE

307 ### 4.1.1 Quantity and Timing of Peak SWE

308 Our measurements fall into four categories based on aspect (north, south) and burn
309 condition (burned, unburned). Bulk snowpack density from snow surveys exhibited similar
310 temporal trends on all aspects throughout the observation period. The average density on burned
311 north aspects was ~10% greater than unburned north aspects and ~15% greater on burned south
312 aspects compared to unburned south aspects (Figure 2a). Density in the burned and unburned
313 areas were consistently similar between north and south aspects with the greatest variability in
314 density occurring within the unburned areas.

315 The median SWE of the probe transects was greater on both north and south aspects in
316 the burned area relative to the same aspect in the unburned area throughout the accumulation
317 period except for 28 November and 28 December on south aspects (Figure 2b and Figure 2c).
318 However, median probe-derived SWE was only significantly different (Wilcoxon t-test; $p <$
319 0.05) between burned and unburned areas for one survey date on north aspects and four survey
320 dates on south aspects during this period (Figure 2b and Figure 2c). Median probe-derived SWE
321 was significantly greater ($p < 0.05$) on north aspects relative to south aspects in both the burned
322 (54% greater SWE) and unburned (59% greater SWE) areas. We also found burned north aspects
323 held a mean 19% less SWE than unburned north aspects for all survey dates, while burned south
324 aspects were 16% lower than unburned south aspects. Additionally, we found the difference in
325 median interquartile range (IQR) of probe-derived SWE was significantly greater ($p < 0.05$) on
326 north burned aspects relative to north unburned areas, and on north aspects compared to south
327 aspects within the burned area during accumulation.

328 For the majority of aspect/burn categories, the AWS and camera-derived SWE was
329 comparable to the median probe-derived SWE measurements during the accumulation period
330 (less than 13% median absolute difference). The one exception was the burned north aspect
331 (camera) site which consistently had greater SWE (25% median absolute difference), likely due
332 to wind deposition and the persistence of early season snow (Figure 2b and Figure 2c).

333 The burned south aspect camera site (Burned–South Camera) reached peak SWE on 15
334 April, 22 days earlier than the other four sites (Burned–North Camera, Burned AWS, Unburned
335 AWS, and Unburned–North Camera), which reached peak SWE on 7 May (Figure 2b and Figure
336 2c). Probe snow depths collected on 6 May show the north burned transect had accumulated 19
337 mm (3%) more SWE than the north unburned transect, while south burned aspects had 34 mm
338 (9%) less SWE than unburned south sites (Figure 2b and Figure 2c). Around the time of peak
339 SWE at the Burned–South Camera, the burned south aspect snow survey on 6 April had 9 mm
340 (2%) greater peak SWE than the snow survey near peak SWE on the unburned south aspect (6
341 May). However, these observed differences in peak SWE were not statistically significant ($p <$
342 0.05). After peak SWE was reached on the burned south aspect but prior to ablation at all other
343 aspects (yellow period in Figure 2b and Figure 2c), SWE declined at a rate of 4 mm d^{-1}. In
344 contrast, burned north, and unburned north and south locations gained SWE at 2, 3, and 1 mm d^{-1}
345 during this period.

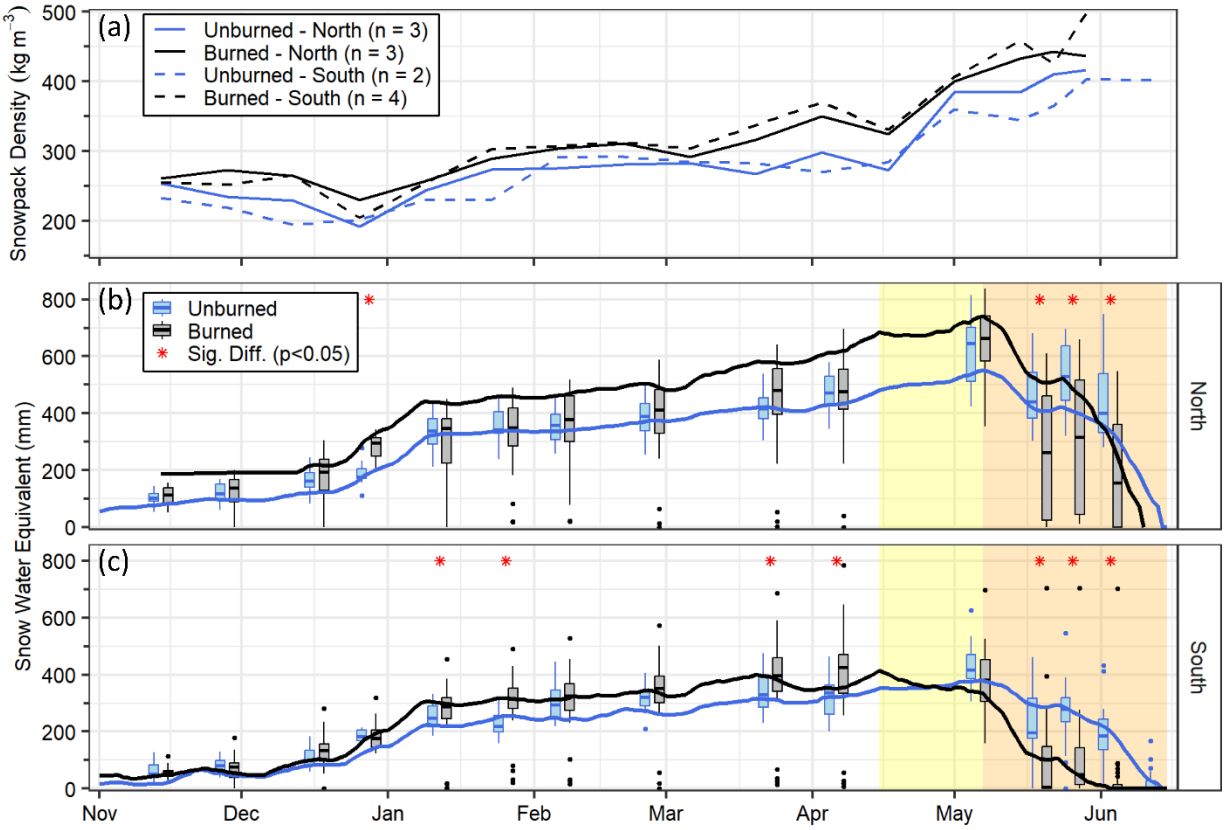

Figure 2. (a) Mean density for each aspect and burn condition calculated from the snow pit and SWE tube bulk densities. The number of sites included for each aspect and burn condition is indicated in the legend. Probe-derived and continuous SWE based on burn condition for (b) north and (c) south aspects. Wilcoxon significant difference of medians between burned and unburned areas are indicated with the red asterisks ($p < 0.05$). The period between burned south peak SWE (15 April) and all other sites peak SWE (7 May) is shown in yellow. The melt period for all sites is shown in orange. Note: Burned-north SWE until mid-December is calculated from snow pit observations only.

4.1.2 Melt Patterns

The differences in snowpack properties between the burned and unburned sites were most apparent during the melt period. Between peak SWE (7 May for most categories) and 20 May, when a five-day storm cycle began which added ~30 cm snow depth, the mean melt rates at the burned north and south sites were both 19 mm d^{-1}, while unburned north and south aspects were 12 and 8 mm d^{-1} (Figure 3a and Figure 3b). Between probe surveys on 6 May and 19 May, the average daily rate of SWE loss in the burned areas (31 mm d^{-1} north; 29 mm d^{-1} south) was approximately double unburned areas (16 mm d^{-1} north; 17 mm d^{-1} south; Figure 3a and Figure 3a). Between the 26 May to 3 June probe surveys, north unburned areas lost 16 mm d^{-1} and south unburned areas lost 11 mm d^{-1}, while in the burned areas, north aspects lost 20 mm d^{-1} and south aspects lost 6 mm d^{-1} (Figure 3a and Figure 3a).

366 On the probe survey dates of 19 May, 26 May, and 3 June, the median difference
367 between burned and unburned transects were 178, 213, and 244 mm on north aspects and 192,
368 231, 186 mm on south aspects (Figure 2b and Figure 2c). While differences between comparable
369 aspects in the burned and unburned areas were similar during this period, median SWE was
370 lower on burned south aspects (0–49 mm) than on burned north aspects (157–316 mm). During
371 the melt period, the IQR expanded on burned north aspects (Figure 2b), with the burned north
372 IQR growing 246 mm (78%) greater than the IQR on unburned north aspects. Similarly, burned
373 south IQR was 32 mm (29%) greater than comparable unburned areas.

374 Snow disappearance occurred on south burned aspects 3 June and on north burned
375 aspects on 10 June, while all unburned sites became snow free on 14 June (Figure 2b and Figure
376 2c). The steeply sloped south aspects (low northness values) were snow free on 19 May, prior to
377 the 5-day spring snowstorm, and became snow free for the season on 1 June following several
378 small storms in late May.

379 4.2 Snowpack Cold Content

380 Snowpack cold content exhibited a distinctive seasonal pattern, with an increase in cold
381 content from November through January, maximum cold content in early February, followed by
382 a decline until all sites were isothermal in early May (Figure 3c). Cold content was greatest on
383 the north burned aspect through 27 December, while the three other sites were similar (Figure
384 3c). Beginning with the 24 January survey, cold content showed greater similarities based on
385 aspect rather than burn condition, with north aspects having greater cold content than south
386 aspects (Figure 3c). All sites reach a maximum cold content during the 9 February survey.
387 Aspect-driven similarities continued until 21 March when snowpack cold content in the burned
388 areas decreased at a greater rate than unburned areas. All sites were isothermal at 0^{o}C on the 7
389 May survey (Figure 3c).

390 4.3 Wind Speed Following Wildfire

391 Wind speeds at the burned site AWS were generally higher than those at the unburned
392 AWS. Specifically, the burned AWS recorded median seasonal windspeeds of 1.76 m s^{-1} while
393 the wind speeds at the unburned AWS were significantly lower ($p < 0.05$; 0.45 m s^{-1}). At the
394 burned AWS, 40% of all hourly windspeeds were greater than 2 m s^{-1} while there were no
395 occurrences greater than 2 m s^{-1} at the unburned AWS (Figure 3d and Figure 3e). Predominant
396 wind directions were south–southwest at both sites (Figure 3d and Figure 3e).

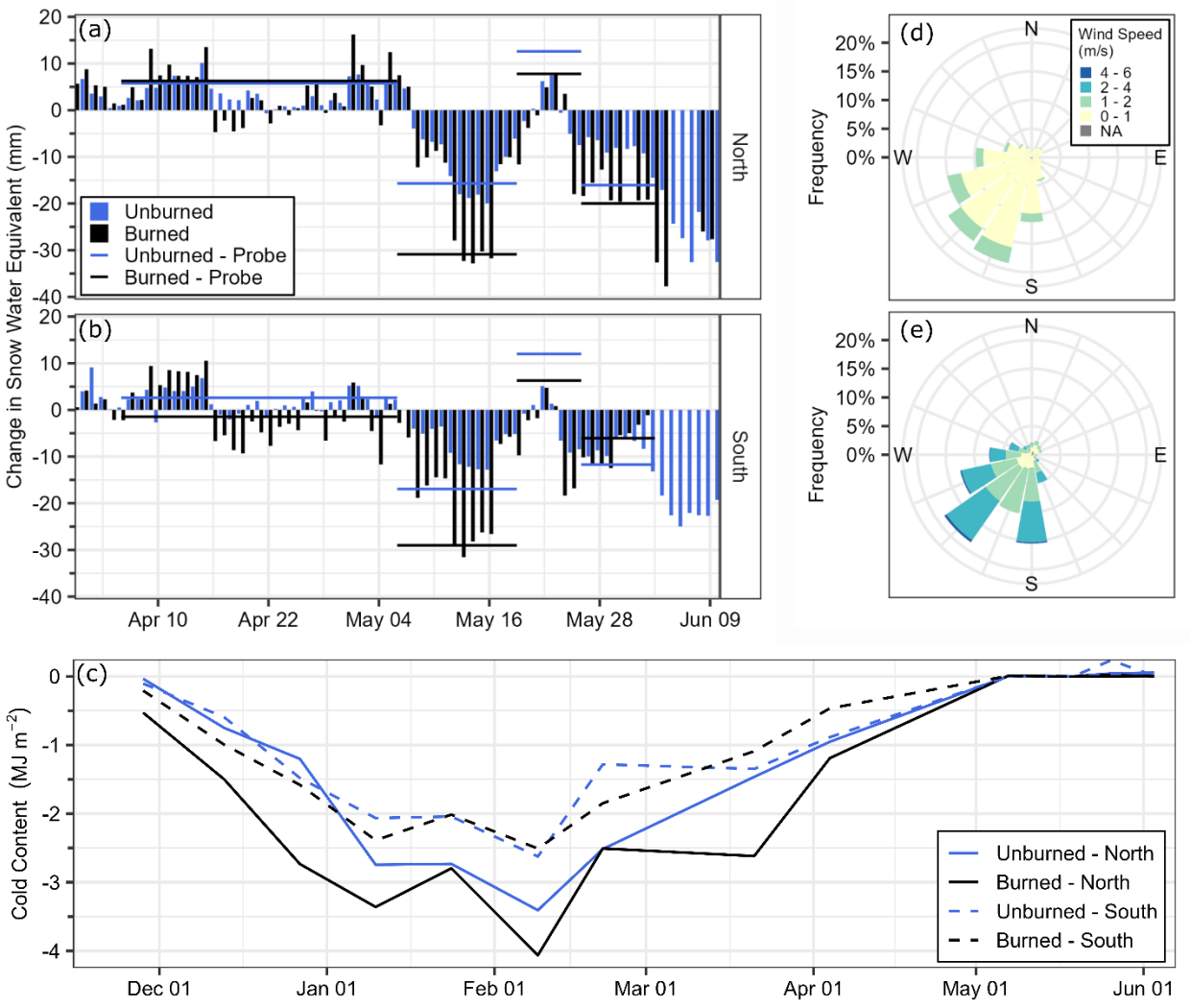

Figure 3. Mean daily change in SWE based on burn condition for (a) north and (b) south aspects. The bars represent the daily change at each of the continuous sites while the horizontal bars show the average daily SWE change between probe surveys. (c) Timeseries of the mean snowpack cold content based on aspect and burn condition. Wind rose showing hourly windspeed and direction for each weather station, (d) unburned AWS and (e) burned AWS.

4.4 Energy Balance Following Wildfire

Since wildfire directly alters forest structure and canopy, all aspects of the snowpack energy balance are impacted following wildfire. Below we present results for the energy balance components (Eqn. 3), based on observations from the burned and unburned AWS sites.

4.4.1 Shortwave Radiation (K)

Mean daily net shortwave radiation was low (47 W m^{-2} burned; 31 W m^{-2} unburned) from 1 December through 28 February, then gradually increased to maximum values of 133 W m^{-2} (burned) and 59 W m^{-2} (unburned) from 1 March through 31 May. The burned site consistently received significant increases ($p < 0.05$) in mean net shortwave radiation relative to the unburned

site (Figure 4a). The magnitude of this increase in net shortwave radiation varied seasonally, with a greater increase in the spring than in mid-winter. The average mean daily incoming shortwave radiation at the burned site was 52% greater than the unburned site from 1 December to 28 February, and 125% greater during the spring (1 March–31 May; Figure 4a). Cumulative mean daily incoming shortwave energy was ~200% greater at both sites during the spring period than during mid-winter. However, the cumulative mean daily net shortwave energy was 56% greater at the burned site than the unburned site through the mid-winter (4 kW m^{-2} burned; 2.5 kW m^{-2} unburned) and 137% greater during the spring (12 kW m^{-2} burned; 5 kW m^{-2} unburned). In total, there was a 110% increase in cumulative mean daily net shortwave radiation between 1 December and 31 May at the burned site relative to the unburned site.

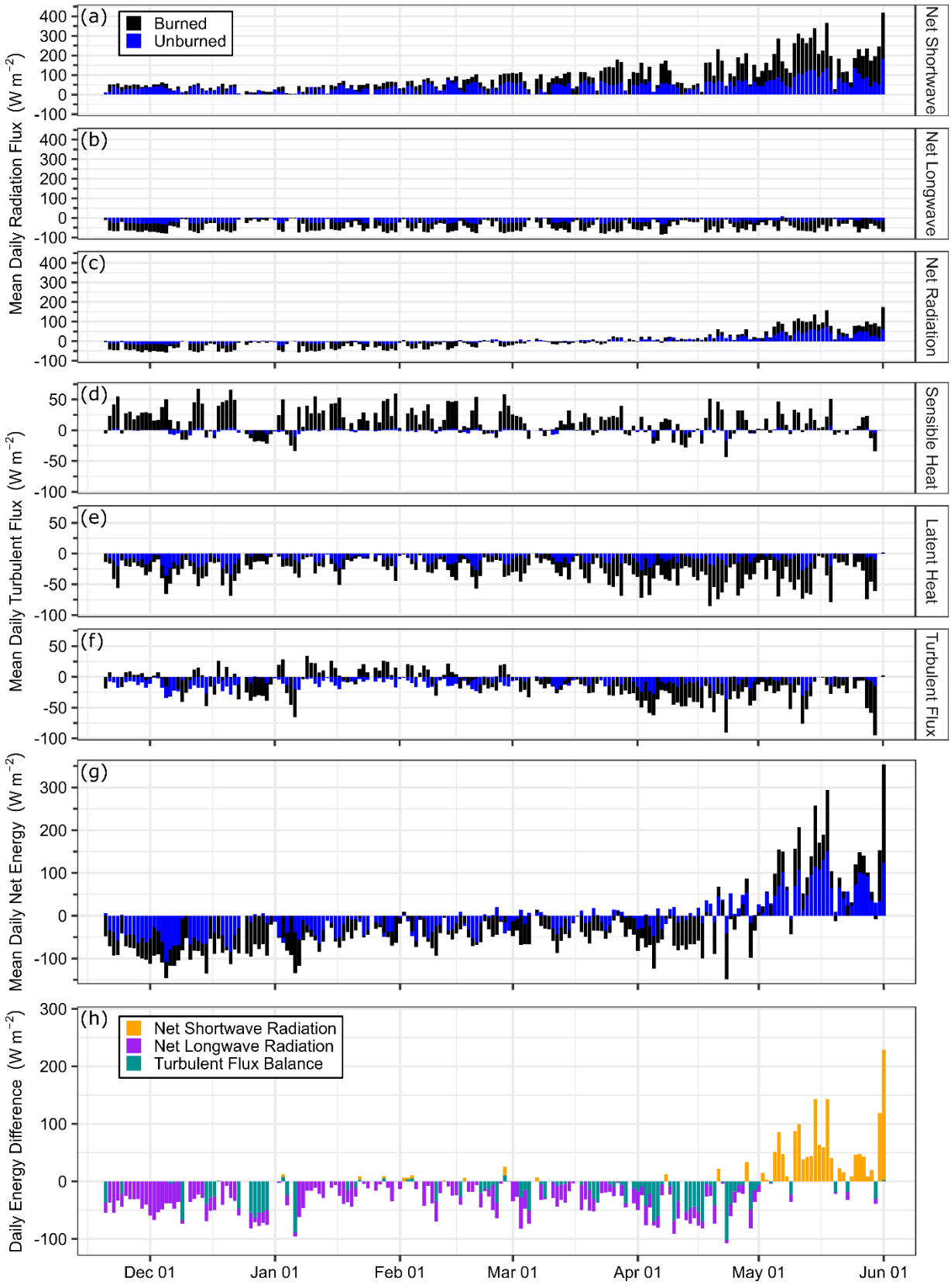
(a)
Burned
Unburned
Net Shortwave
(b)
Net Longwave
(c)
Net Radiation
Mean Daily Radiation Flux (W m^{-2})
(d)
Sensible Heat
(e)
Latent Heat
(f)
Turbulent Flux
Mean Daily Turbulent Flux (W m^{-2})
(g)
Mean Daily Net Energy (W m^{-2})
(h)
Net Shortwave Radiation
Net Longwave Radiation
Turbulent Flux Balance
Daily Energy Difference (W m^{-2})
Dec 01
Jan 01
Feb 01
Mar 01
Apr 01
May 01
Jun 01

422

Figure 4. (a) Mean daily net shortwave, (b) longwave, and (c) radiation flux for the burned and unburned AWS sites. Mean daily (d) sensible, (e) latent, and (f) total turbulent heat fluxes for the burned and unburned AWS sites. (g) mean daily net energy at the burned and unburned AWS sites. (h) Daily difference between the mean daily net energy at the burned and unburned sites (burned minus unburned), and the proportion of the net difference attributed to each energy balance component.

4.4.1.1 Snow Surface Albedo

The median broadband albedo (upward-looking, 385 nm to 2105 nm; downward-looking, 295 nm to 2685 nm) at the unburned AWS (0.53) was 29% lower than the median burned albedo (0.74) from 1 December through 28 February (Figure 5a). The median albedo remained greater at the burned site (0.69) than the unburned site (0.55) between 1 March and 31 May. However, median snow surface albedo changed rapidly at both sites between 1 May and 15 May with the albedo at the burned site falling from 0.67 to 0.36 while the unburned albedo fell from 0.54 to 0.30. Both sites rebounded to 0.67 (burned) and 0.54 (unburned) during the late-May storm cycle, before falling to 0.16 (burned) and 0.33 on 1 June.

We collected distributed spectral albedo measurements on 15 May, however, a strong low-pressure system in mid-April led to the wet deposition of dust at all sites (Figure 5c and Figure 5d). Comparing the spectral albedo on 15 May, we found the spectral albedo in the burned area was 37% less ($p < 0.05$) than the spectral albedo in the unburned areas across all measured wavelengths (350–2500 nm; Figure 5b). In the visible wavelengths (400–700 nm), we found there to be a significant difference ($p < 0.05$) in the median albedos – the burned area albedo (0.44) was 42% lower than the unburned area albedo (0.76). In the measured NIR spectrum (700–2500 nm), the burned area median albedo (0.14) was 26% less ($p < 0.05$) than the unburned area (0.19).

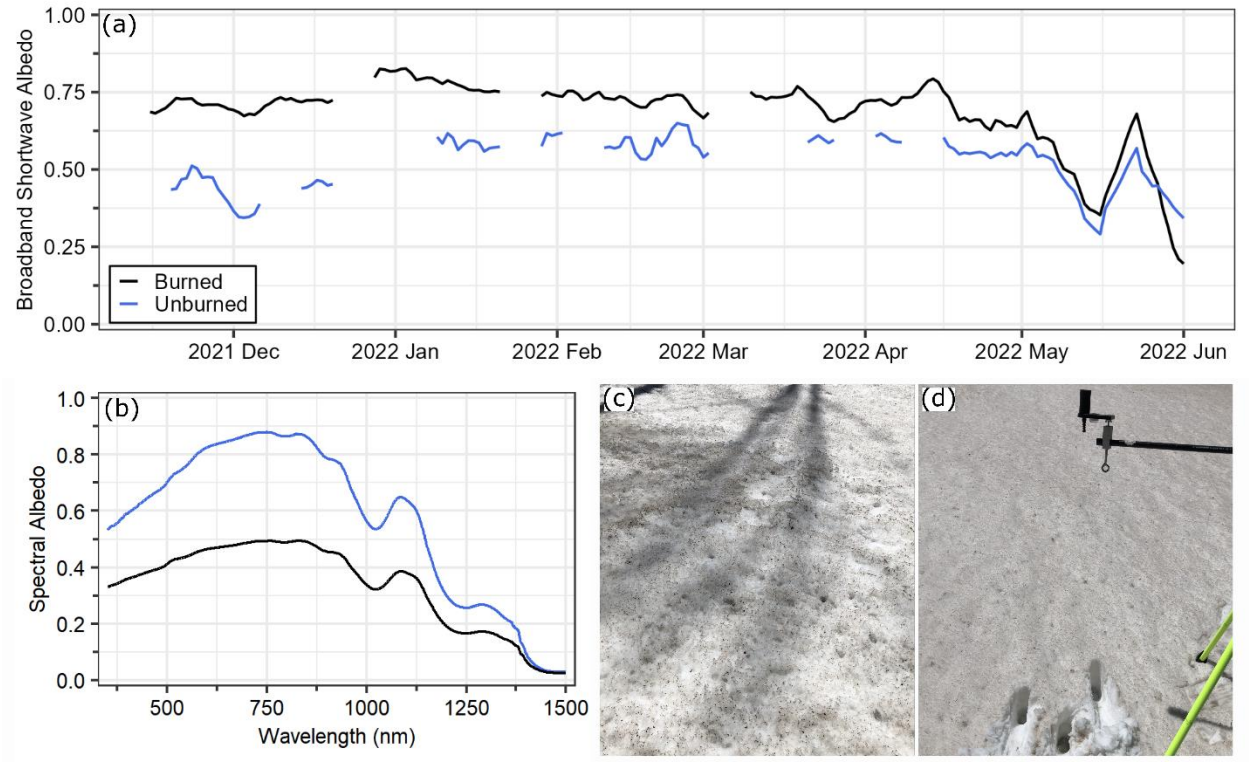

Figure 5. (a) Seven-day rolling mean of broadband (upward-looking, 385 nm to 2105 nm; downward-looking, 295 nm to 2685 nm) albedo at the burned and unburned automated weather stations. Albedo was calculated as the median value between 1000 and 1400 hours. (b) Spectral albedo in burned and unburned locations on 15 May. (c) Snow surface at a burned ASD measurement location. (d) Unburned snow surface and the ASD remote cosine receptor and tripod. Note: Snow samples were taken after all measurements were collected.

4.4.2 Longwave Radiation (L)

Differences in mean daily net longwave radiation between the sites was more temporally consistent than shortwave radiation, as the burned site was always more negative. Between December through February, the burned site balance was –46 W m^{-2}, while the unburned was –16 W m^{-2} and between March through May, the burned site was –45 W m^{-2} whereas the unburned was –13 W m^{-2} (Figure 4a and Figure 4b).

This difference in net longwave was primarily due to differences in incoming longwave radiation between the sites. During mid-winter (1 December–28 February), there was a 16% decrease in cumulative mean daily incoming longwave ($p<0.05$) at the burned site relative to the unburned site, while in the spring (1 March–31 May) there was a 14% decrease at the burned site compared to the unburned site. Cumulative mean daily outgoing longwave radiation was lower at the burned area by 4% during the mid-winter period and 2% during the spring period compared to the unburned site.

4.4.3 Net Radiation Flux (R)

The direction of energy flux between the snowpack and atmosphere varied seasonally at both the burned and unburned AWS sites. From 1 December through 28 February, the net radiation flux was negative on approximately 92% of days at the burned AWS and 74% of days at the unburned AWS site (Figure 4c). Between 1 March and 31 May, net radiation was positive on 76% and 81% of days at the burned and unburned AWS sites, respectively. The magnitude of net radiation flux was primarily a function of burned/unburned condition. Specifically, between 1 December and 28 February, the cumulative mean daily net radiation at the burned site (–2.5 kW m^{-2}) was 2 kW m^{-2} (360%) more negative than the unburned site (–0.5 kW m^{-2}; Figure 4f). From 1 March through 31 May, the cumulative net radiation at the burned site (2.7 kW m^{-2}) was 1.2 kW m^{-2} (77%) greater than the unburned site (1.5 kW m^{-2}).

4.4.4 Turbulent Heat Fluxes (H, L_vE)

Turbulent fluxes also varied based on the season at both sites. The average mean daily sensible heat flux at the burned AWS was 19 W m^{-2} (snowpack gained energy) between 1 December and 28 February, while at the unburned site, the sensible heat flux was –1 W m^{-2} (snowpack lost energy; Figure 4d). During the spring, the magnitude of average daily sensible heat flux decreased at both the burned (8 W m^{-2}) and unburned sites (–0.5 W m^{-2}; Figure 4d). The magnitude of average daily latent heat flux increased from the winter to the spring at the burned site (–22 W m^{-2} winter; –34 W m^{-2} spring) but decreased slightly at the unburned sites (–9 W m^{-2} winter; –7 W m^{-2} spring; Figure 4e).

Both sensible and latent heat fluxes varied considerably during different weather conditions, with the lowest magnitude sensible and latent heat fluxes during periods of snowfall and the greatest values during periods of high pressure. From 1 December to 31 May, sensible heat flux added a cumulative total of 2.4 kW m^{-2} at the burned site while the unburned site lost 0.1 kW m^{-2}, while the cumulative latent heat flux removed energy from both sites (–5.2 kW m^{-2} burned; –1.5 kW m^{-2} unburned). In general, the magnitude of latent fluxes exceeded sensible fluxes, causing the net turbulent flux to be negative on 78% of the days during the study period at the burned site, 90% at the unburned. In the burned area, increased daily turbulent flux led to a greater loss of cumulative turbulent energy at the burned site (–2.8 kW m^{-2}) compared to the unburned site (–1.6 kW m^{-2}).

4.4.5 Daily Net Energy (Q)

The daily net energy at both the burned and unburned sites was consistently negative (99% of days at the burned; 100% unburned) from 1 December through 28 February. During this time, the cumulative mean daily net energy was –5.5 kW m^{-2} and –2.8 kW m^{-2} at the burned and unburned sites (96% greater deficit). From 1 March through 31 May, the daily mean net energy was positive on 62% of days at the unburned site but only 31% at the burned site. The daily mean net energy became consistently positive at the unburned site on 14 April and at the burned site on 1 May (Figure 4f). Before 14 April, the differences between burned and unburned areas were primarily due to changes in the net longwave and turbulent flux components of the energy balance, which reduced the energy balance in the burned area compared to the unburned area (Figure 4g). The primary component of the difference between the burned and unburned sites then became the net shortwave radiation through April and May, causing the net energy at the burned site to become greater than at the unburned site (Figure 4g). Between 14 April and 31

May at the burned site, the increased net shortwave radiation at the burn site drove a 19% greater cumulative mean energy balance at the burned site (2.6 kW m^{-2}) compared to the unburned site (2.2 kW m^{-2}). During May alone, the cumulative mean energy balance was 59% greater in the burned area than the unburned area.

5 Discussion

5.1 Snowpack Accumulation and Ablation

5.1.1 Peak SWE Timing and Quantity

Our results highlight the important, but nuanced, role of aspect on the timing of peak SWE. At the burned south site, peak SWE occurred 22 days earlier than the unburned south site, while this date was the same for burned/unburned north aspects. These timing changes are outside the average 6–10 day range reported in previous literature for the western U.S (Smoot and Gleason, 2021; Giovando and Niemann, 2022). One possible explanation for the difference on south aspects is that previous studies examined SNOTEL sites which are typically in open meadows with low surface slopes, while our sites have slopes between 2 and 24 degrees. Continued study over multiple years would help illuminate whether the coincident peak SWE date on north aspects was due to synoptic scale weather patterns or if peak SWE is minimally affected post-fire on north slopes.

Additionally, we found no difference in peak SWE magnitude between our probe snow surveys in burned and unburned areas (Figure 2). This finding differs from previous western U.S. studies, which have reported decreases of 10 to 50% in peak SWE post-fire (Harpold et al., 2014; Smoot and Gleason, 2021; Giovando and Niemann, 2022). Additionally, these results differ from 2020–2021 winter observations within the same study area where peak SWE was 17–25% less in burned sites relative to unburned sites (Kampf et al., 2022; McGrath et al., 2023). The discrepancies in peak SWE between the 2020–2021 and 2021–2022 winters within the study area could represent sensitivity to interannual snow accumulation patterns. Although both winters were average when compared to the 30-year median, snow accumulated consistently during the 2020–2021 winter, while the 2021–2022 winter was characterized by long dry periods punctuated by short periods of rapid snow accumulation. Additionally, the use of more automated sites and more extensive probe transects during the 2021–2022 winter could have contributed to the observed differences. In contrast to the differences in peak SWE between the 2020–2021 and 2021–2022 winters in this study area, the change in SDD between burned and unburned areas (7–11 days) was consistent between the years (11–13 days; McGrath et al., 2023), and were similar to the average for the Southern Rockies (11.7 days; Giovando and Niemann, 2022), but are less than the 23 days reported by Gleason et al. (2013) from the High Cascades.

5.1.2 Aspect Influence

While we found increased impacts on south aspect slopes and earlier melt dates within the burned area, the greatest difference in SWE accumulation and melt rates occurred based on aspect regardless of the burn condition. This finding matches the previous literature in burned and unburned forests who illustrate the variability in SWE accumulation and ablation patterns based on aspect and canopy cover (Anderson et al., 2014; Maxwell et al., 2019; Moeser et al.,

2020). Following peak SWE, melt rates increased in the burned areas on both north and south slopes, with the greatest increases occurring on burned south aspects (Figure 6). The increased average daily probe-derived melt rates in the burned areas prior to the late-May snowstorm and the earlier peak SWE on burned south slopes caused earlier snow disappearance in the burned area on all aspects (Figure 6). On these south-facing slopes, the growing season is lengthened due to the earlier snow-free dates, but the growth of revegetation may be water limited, slowing recovery of forest canopy following wildfire (Stevens-Rumann and Morgan, 2019; Webb et al., 2023).

We found that the north burned aspects held consistently greater snow depths during the probe snow depth surveys throughout the entire study period. To investigate this further, we analyzed Sentinel-2 and Landsat-8 satellite imagery from late fall 2022, which revealed that accumulation from an early October snowstorm had completely melted from burned south aspects by 25 October but was still present on burned north aspects. The presence of forest canopy made observations in unburned areas inconclusive, but it appeared that steep south-facing unburned slopes had melted completely, while all other unburned slopes retained snow. While we do not know the depth of snow that remained, we attribute the relatively consistent difference in snow depth identified throughout the accumulation period to aspect-dependent energy balance differences following this early season snowfall along with preferential wind deposition of snow to this area during accumulation, which was observed during the periodic site visits.

5.2 Snowpack Energy Balance

While prior studies have documented changes to peak SWE, peak SWE date, melt rates, and SDD, few studies have directly compared all components of the energy balances between burned and unburned sites. We found that incoming shortwave radiation increased significantly at the burned site compared to the unburned site and the magnitude of this difference increased through the season as the length of day and zenith angle increased. The increased incoming shortwave radiation resulted in a 110% increase in cumulative mean net shortwave radiation at the burned site compared to the unburned site between 1 December and 31 May (Figure 6a and Figure 6b).

This increase in net shortwave radiation was primarily due to the loss of canopy, which dramatically increased the magnitude of shortwave radiation reaching the snow surface. Like Gleason and Nolin (2016), we observed a higher albedo at the burned site compared to the unburned site during the accumulation period. We attribute the lower albedo in the unburned site during the accumulation period to two factors: i) the accumulation of leaf litter on the snow surface (Figure S3), and ii) the integrated signal from both snow and trees within the sensor's field of view. During the peak melt season, the burned site had a slightly lower minimum albedo but unlike previous studies (e.g., 40% and 60% decreases identified by Gleason and Nolin (2016) and Hatchett et al. (2023) during melt), our stations did not document a comparable precipitous decline in snow albedo. The darkening of the snow surface from fallen soot and debris post-fire relative to unburned conditions (Burles and Boon, 2011; Gleason et al., 2013, 2022; Gleason and Nolin, 2016; Gersh et al., 2022) was potentially minimized at our study site due to a widespread dust on snow event that affected all areas equally, as well as a late-season snowstorm that

increased the albedo across all sites for a ~5-day period in late May. These late season events are a common occurrence for this eco-region (e.g., McGrath et al., 2023).

In contrast to the station data, the spectroradiometer observations that were collected on 15 May revealed more distinct differences between the burned and unburned sites. Visible wavelength albedo at the burned sites were 42% less than comparable unburned areas, which is comparable to previous studies, including the 40% decline found during prior winter (the first post-fire) at this site (McGrath et al., 2023). These observations coincided with a period in the melt season when the burned station albedo was 18% greater than the unburned site.

Importantly, as wildfires lead to the loss of canopy, snow albedo plays an outsized role in the snowpack's post-fire energy balance due to the dramatic increases in incoming shortwave radiation reaching the snow surface. Although our station data did not show a consistent decline in snow albedo, the loss of canopy in the burned area, coupled with a low albedo during the melt period, led to a 110% increase in cumulative net shortwave energy, highlighting the transformative and long-lasting role that fires can have on the snowpack energy balance.

Unlike net shortwave radiation, the net longwave radiation difference between the burned and unburned sites was consistent throughout the entire study period, which is attributed to the loss of tree canopy at the burn site. Trees absorb shortwave radiation and re-emit longwave radiation (Rouse, 1984), so the loss of canopy greatly reduced incoming longwave radiation and shifted net longwave markedly more negative at the burned site. We have observed consistent melt-out patterns in the burned site during the first two winters post-fire, where snow first disappears in the immediate vicinity of the remaining trunks before expanding radially (Figure S2). While this pattern could be the result of lower snow accumulation or a more positive shortwave balance due to a lower albedo, we hypothesize that the remaining trunks are a major longwave energy source, therefore modifying the energy balance in the immediate vicinity of the trees in a way that is not being accurately captured by the station data.

The seasonal variability in the magnitude of net shortwave radiation differences drove the seasonally dependent net radiation differences between burned and unburned areas. This seasonality is highlighted by the more negative net radiation in the burned area through the winter, followed by a more positive net radiation balance during the spring. These results emphasize the importance of the increased shortwave radiation incident on the snowpack following wildfire in the Southern Rockies, but also that increased longwave radiation losses partially counter this increase, particularly leading up to March. The pronounced difference in net radiation following 1 March underscores the importance for management solutions that have been shown to reduce the severity of wildfire and improve the likelihood of tree regeneration following the disturbance so that forests regrow, reducing the likelihood of permanent alterations to forest vegetation, particularly on southerly aspects and steep slopes (Rother and Veblen, 2016; Stevens-Rumann and Morgan, 2019; Rodman et al., 2020; Davis et al., 2023; Webb et al., 2023).

The net energy was a story of two seasons for both the burned and unburned sites with the change in sign occurring at the burned site later than at the unburned site. The daily and cumulative net energy became positive at the burned site approximately one week after the unburned site. This difference is driven mainly by the increased magnitude of net longwave radiation losses which required additional incoming shortwave energy to flip the direction of the

net energy. This early season difference in net energy manifested as greater early season cold content in the burned area snowpacks compared to the unburned snowpacks through mid-March. The increased cold content in the burned snowpacks during the early portion of the season could be a result of the more negative net longwave radiation observed at the burned sites, which is primarily attributed to the widespread loss of biomass in these locations. However, net energy may not always be a reliable indicator of snowpack cold content, as cold content integrates both mass and energy balance components. At our sites, cold content and net energy become decoupled in mid-February with the snowpack steadily losing cold content (i.e., gaining energy) while the net energy balance was still negative (Figure 2 and Figure 3). The pattern of snowpack cold content development we identified early in the season follows the findings of Jennings et al. (2018), who found that cold content was primarily developed through new snowfall. From mid-December until mid-January we saw rapid snowpack and cold content development within all four aspect and burn categories. Yet, from mid-February through mid-April our snow pit data indicated a decline in cold content although the net energy balance was negative, suggesting increases in cold content. Snow accumulation (i.e., mass gain) slowed substantially during this period, with long dry periods between storms, which may have played a role in the decoupling of cold content and the net energy balance.

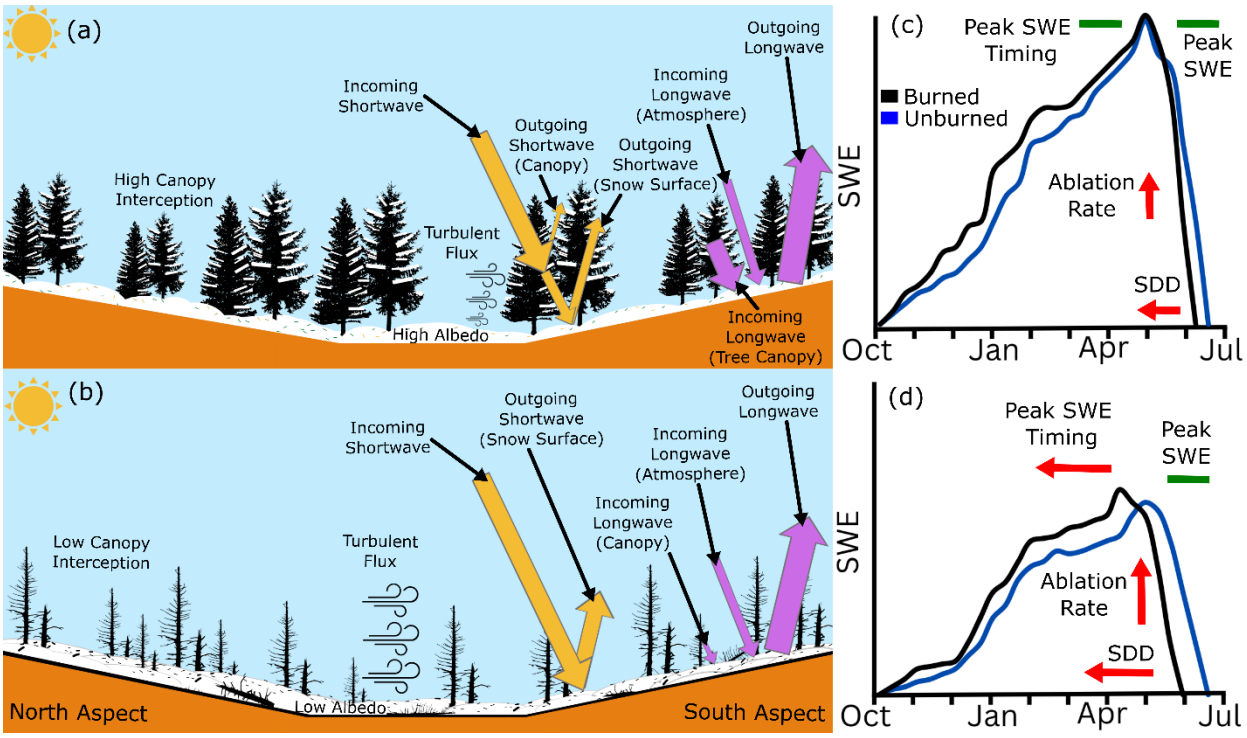

Figure 6. Snowpack energy balance for a clear-sky, daytime condition (a) without wildfire and (b) following wildfire based on aspect where arrow and icon size represents relative change. Changes in the snowpack mass balance and timing on (c) north and (d) south burned aspects where blue indicates unburned areas, black is burned areas, arrow size indicates the magnitude of the change following wildfire, and horizontal bars indicate no significant difference between the unburned and burned areas.

660 5.2.1 Influence of Snow Regime

661 Our observations from a continental snow regime may vary from other locations in the
662 western U.S., where accumulation patterns and climate differ. Our study site is characterized by
663 frequent, low magnitude storm events that continue through the melt season, thereby frequently
664 re-setting the snow surface albedo (Figure 2; McGrath et al., 2023). In contrast, in the Sierra
665 Nevada, where storms tend to be less frequent but of larger magnitude, extended periods of high
666 pressure can lead to the accumulation of soot/debris on the snow surface. This lower albedo can
667 lead to significant mid-winter melt within wildfire burned areas as shown by Hatchett et al.
668 (2023). In areas like the Pacific Northwest, longwave energy can dominate the energy balance
669 and regulate the timing and rate of snow melt (Kraft et al., 2022). In these areas, the loss of
670 longwave energy from the canopy might alter the snowpack similarly to what was observed in
671 this study, where the lack of longwave energy resulted in greater cold content during the early
672 portions of the accumulation season. However, the loss of this canopy could then lead to
673 significantly greater melt rates than pre-wildfire due to a shift from longwave to shortwave
674 radiation as the dominant energy balance component (Uecker et al., 2020). As fires increasingly
675 impact seasonal snowpacks that accumulate in high-elevation forests (Kampf et al., 2022), it is
676 imperative that we develop a thorough understanding of how snow regime and climate modulate
677 snow accumulation and melt patterns post-fire.

678 **5 Conclusions**

679 Using season-long paired in-situ and automated weather station measurements, we
680 investigated the mass and energy balance impacts following wildfire to a high-elevation seasonal
681 snowpack in complex terrain. Our research shows that complex terrain in post-wildfire burned
682 areas can modulate the impacts of the wildfire, with south burned aspects showing the greatest
683 impact to peak SWE timing, melt rates, and snow disappearance date. This comparison indicated
684 that south aspect burned areas reached SDD at least 11 days before south unburned aspects while
685 burned north aspect SDD occurred 4 days earlier to similar unburned areas. We found no
686 significant difference in peak SWE quantity between burned and unburned areas with similar
687 aspects.

688 Through a comparison of the paired AWS data, we found that the net energy at the
689 burned site was significantly different than the unburned site over the entire winter season,
690 however the sign of that change varied across the season. During the winter (before 1 March),
691 the loss of energy from net longwave and net turbulent fluxes resulted in a significantly more
692 negative net energy at the burned site compared to the unburned site. However, following 1 May,
693 the energy balance at the burned site surpassed the unburned site due to the increased shortwave
694 energy that was available and absorbed by the burned snowpack.

695 Incorporating aspect-based analysis of SWE accumulation and melt following wildfire
696 and paired energy balance analysis between burned and unburned areas furthers our
697 understanding of how wildfire alters the physical processes within high-elevation seasonal
698 snowpacks. This work will allow for better operational and scientific understanding of hydrology
699 following wildfire in snow dominated watersheds, which is essential due to the importance of
700 these snowpacks for downstream water users and the rapid increases in wildfire at these
701 elevations since 2000 (Alizadeh et al., 2021; Iglesias et al., 2022; Kampf et al., 2022). By
702 analyzing the alteration of the mass and energy balances following wildfire across complex

703 terrain within a high-elevation continental snow zone, our research provides a nuanced
704 assessment of these impacts that can help inform decision making for water resource and
705 snowmelt flood risk management following wildfire.

706

Acknowledgments

The authors would also like to first acknowledge, with respect, the significant amount of fieldwork that occurred on the traditional and ancestral lands of the Eastern Shoshone, Ute, Cheyenne, and Arapaho Nations and peoples. This research was funded in part by The Geological Society of America Research Grant, the Colorado State University Evelyn I. Clark and Warner College of Natural Resources Scholarships, the Sigma Xi Research Grant, and the Colorado Mountain Club Foundation Research Grant. We thank Huihui Zhang and Kevin Yemoto with the USDA ARS in Fort Collins, CO for supporting the spectroradiometer observations. Thank you to Amber Scott, John Kemper, Lucas Zeller, Megan Sears, Aly Cheney, Anna Marshall, Holly Proulx, Tara Vessella, and Lucas Dolliver for their field assistance.

Open Research

The automated weather station, time lapse camera snow depths, and snow pit and snow probe data used for the mass and energy balance analysis in the study are available at HydroShare via https://www.hydroshare.org/resource/868df9f8bdac495e876fb36220eb0f9d/.

References

Alizadeh, M. R., Abatzoglou, J. T., Luce, C. H., Adamowski, J. F., Farid, A., and Sadegh, M. (2021). Warming enabled upslope advance in western US forest fires. *Proc Natl Acad Sci U S A* 118. doi: 10.1073/pnas.2009717118.

Anderson, B. T., McNamara, J. P., Marshall, H.-P., and Flores, A. N. (2014). Insights into the physical processes controlling correlations between snow distribution and terrain properties. *Water Resour Res* 50, 4545–4563. doi: 10.1002/2013WR013714.

Andreas, E. L. (2002). Parameterizing Scalar Transfer over Snow and Ice: A Review.

Bales, R. C., Molotch, N. P., Painter, T. H., Dettinger, M. D., Rice, R., and Dozier, J. (2006). Mountain hydrology of the western United States. *Water Resour Res* 42. doi: 10.1029/2005WR004387.

Barnett, T. P., Adam, J. C., and Lettenmaier, D. P. (2005). Potential impacts of a warming climate on water availability in snow-dominated regions. *Nature* 438, 303–309. doi: 10.1038/NATURE04141.

Barnhart, T. B., Molotch, N. P., Livneh, B., Harpold, A. A., Knowles, J. F., and Schneider, D. (2016). Snowmelt rate dictates streamflow. *Geophys Res Lett* 43, 8006–8016. doi: 10.1002/2016GL069690.

Biederman, J. A., Brooks, P. D., Harpold, A. A., Gochis, D. J., Gutmann, E., Reed, D. E., et al. (2014). Multiscale observations of snow accumulation and peak snowpack following widespread, insect-induced lodgepole pine mortality. *Ecohydrology* 7, 150–162. doi: 10.1002/eco.1342.

Boon, S. (2009). Snow ablation energy balance in a dead forest stand. *Hydrol Process* 23, 2600–2610. doi: 10.1002/hyp.7246.

Brutsaert, W. (1982). *Evaporation into the Atmosphere*. Dordrecht: Springer Netherlands doi: 10.1007/978-94-017-1497-6.

Burles, K., and Boon, S. (2011). Snowmelt energy balance in a burned forest plot, Crowsnest Pass, Alberta, Canada. *Hydrol Process* 25, 3012–3029. doi: 10.1002/hyp.8067.

Cayan, D. R., Dettinger, M. D., Kammerdiener, S. A., Caprio, J. M., and Peterson, D. H. (2001). Changes in the Onset of Spring in the Western United States. *Bull Am Meteorol Soc* 82, 399–415. doi: 10.1175/1520-0477(2001)082<0399:CITOOS>2.3.CO;2.

Clow, D. W. (2010). Changes in the timing of snowmelt and streamflow in Colorado: A response to recent warming. *J Clim* 23, 2293–2306. doi: 10.1175/2009JCLI2951.1.

Davis, K. T., Robles, M. D., Kemp, K. B., Higuera, P. E., Chapman, T., Metlen, K. L., et al. (2023). Reduced fire severity offers near-term buffer to climate-driven declines in conifer resilience across the western United States. *Proc Natl Acad Sci U S A* 120. doi: 10.1073/pnas.2208120120.

Dozier, J. (1980). A clear-sky spectral solar radiation model for snow-covered mountainous terrain. *Water Resour Res* 16, 709–718. doi: 10.1029/WR016i004p00709.

Dudley, R. W., Hodgkins, G. A., McHale, M. R., Kolian, M. J., and Renard, B. (2017). Trends in snowmelt-related streamflow timing in the conterminous United States. *J Hydrol (Amst)* 547, 208–221. doi: 10.1016/j.jhydrol.2017.01.051.

Elder, K., Dozier, J., and Michaelsen, J. (1989). Spatial and Temporal Variation of Net Snow Accumulation in a Small Alpine Watershed, Emerald Lake Basin, Sierra Nevada, California, U.S.A. *Ann Glaciol* 13, 56–63. doi: 10.3189/s0260305500007643.

Elder, K., Dozier, J., and Michaelsen, J. (1991). Snow accumulation and distribution in an Alpine Watershed. *Water Resour Res* 27, 1541–1552. doi: 10.1029/91WR00506.

Gersh, M., Gleason, K. E., and Surunis, A. (2022). Forest Fire Effects on Landscape Snow Albedo Recovery and Decay. *Remote Sens (Basel)* 14. doi: 10.3390/rs14164079.

Giovando, J., and Niemann, J. D. (2022). Wildfire Impacts on Snowpack Phenology in a Changing Climate Within the Western U.S. *Water Resour Res* 58, e2021WR031569. doi: 10.1029/2021WR031569.

Gleason, K. E., McConnell, J. R., Arienzo, M. M., Sexstone, G. A., and Rahimi, S. (2022). Black carbon dominated dust in recent radiative forcing on Rocky Mountain snowpacks. *Environmental Research Letters* 17. doi: 10.1088/1748-9326/ac681b.

Gleason, K. E., and Nolin, A. W. (2016). Charred forests accelerate snow albedo decay: parameterizing the post-fire radiative forcing on snow for three years following fire. *Hydrol Process* 30, 3855–3870. doi: 10.1002/hyp.10897.

Gleason, K. E., Nolin, A. W., and Roth, T. R. (2013). Charred forests increase snowmelt: Effects of burned woody debris and incoming solar radiation on snow ablation. *Geophys Res Lett* 40, 4654–4661. doi: 10.1002/grl.50896.

Hale, K. E., Jennings, K. S., Musselman, K. N., Livneh, B., and Molotch, N. P. (2023). Recent decreases in snow water storage in western North America. *Commun Earth Environ* 4, 170. doi: 10.1038/s43247-023-00751-3.

Hall, D. K., Crawford, C. J., DiGirolamo, N. E., Riggs, G. A., and Foster, J. L. (2015). Detection of earlier snowmelt in the wind river range, wyoming, using landsat imagery, 1972-2013. *Remote Sens Environ* 162, 45–54. doi: 10.1016/j.rse.2015.01.032.

Hammond, J. C., Sexstone, G. A., Putman, A. L., Barnhart, T. B., Rey, D. M., Driscoll, J. M., et al. (2023). High Resolution SnowModel Simulations Reveal Future Elevation-Dependent Snow Loss and Earlier, Flashier Surface Water Input for the Upper Colorado River Basin. *Earths Future* 11, e2022EF003092. doi: 10.1029/2022EF003092.

Hardy, J. P., Davis, R. E., Jordan, R., Li, X., Woodcock, C., Ni, W., et al. (1997). Snow ablation modeling at the stand scale in a boreal jack pine forest. *Journal of Geophysical Research Atmospheres* 102, 29397–29405. doi: 10.1029/96jd03096.

Harpold, A. A., Biederman, J. A., Condon, K., Merino, M., Korgaonkar, Y., Nan, T., et al. (2014). Changes in snow accumulation and ablation following the Las Conchas Forest Fire, New Mexico, USA. *Ecohydrology* 7, 440–452. doi: 10.1002/eco.1363.

Hatchett, B. J., Koshkin, A. L., Guirguis, K., Rittger, K., Nolin, A. W., Heggli, A., et al. (2023). Midwinter dry spells amplify post-fire snowpack decline. *Geophys Res Lett*. doi: 10.1029/2022GL101235.

Iglesias, V., Balch, J. K., and Travis, W. R. (2022). U.S. fires became larger, more frequent, and more widespread in the 2000s. Available at: https://www.science.org.

Jennings, K. S., Kittel, T. G. F., and Molotch, N. P. (2018). Observations and simulations of the seasonal evolution of snowpack cold content and its relation to snowmelt and the snowpack energy budget. *Cryosphere* 12. doi: 10.5194/tc-12-1595-2018.

Kampf, S. K., Mcgrath, D., Sears, M. G., Fassnacht, S. R., Kiewiet, L., and Hammond, J. C. (2022). Increasing wildfire impacts on snowpack in the western U.S. doi: 10.1073/pnas.

Kraft, M., McNamara, J. P., Marshall, H.-P., and Glenn, N. F. (2022). Forest impacts on snow accumulation and melt in a semi-arid mountain environment. *Frontiers in Water* 4. doi: 10.3389/frwa.2022.1004123.

Li, D., Wrzesien, M. L., Durand, M., Adam, J., and Lettenmaier, D. P. (2017). How much runoff originates as snow in the western United States, and how will that change in the future? *Geophys Res Lett* 44, 6163–6172. doi: 10.1002/2017GL073551.

Liston, G. E., Haehnel, R. B., Sturm, M., Hiemstra, C. A., Berezovskaya, S., and Tabler, R. D. (2007). Simulating complex snow distributions in windy environments using SnowTran-3D. *Journal of Glaciology* 53, 241–256. doi: 10.3189/172756507782202865.

Loiselle, D., Du, X., Alessi, D. S., Bladon, K. D., and Faramarzi, M. (2020). Projecting impacts of wildfire and climate change on streamflow, sediment, and organic carbon yields in a forested watershed. *J Hydrol (Amst)* 590, 125403. doi: 10.1016/j.jhydrol.2020.125403.

Maina, F. Z., and Siirila-Woodburn, E. R. (2020). Watersheds dynamics following wildfires: Nonlinear feedbacks and implications on hydrologic responses. *Hydrol Process* 34, 33–50. doi: 10.1002/hyp.13568.

Mandal, A., Angchuk, T., Azam, M. F., Ramanathan, A., Wagnon, P., Soheb, M., et al. (2022). An 11-year record of wintertime snow-surface energy balance and sublimation at 4863ma.s.l. on the Chhota Shigri Glacier moraine (western Himalaya, India). *Cryosphere* 16, 3775–3799. doi: 10.5194/tc-16-3775-2022.

Marshall, A. M., Abatzoglou, J. T., Link, T. E., and Tennant, C. J. (2019). Projected Changes in Interannual Variability of Peak Snowpack Amount and Timing in the Western United States. *Geophys Res Lett* 46, 8882–8892. doi: 10.1029/2019GL083770.

Maxwell, J. D., Call, A., and St. Clair, S. B. (2019). Wildfire and topography impacts on snow accumulation and retention in montane forests. *For Ecol Manage* 432, 256–263. doi: 10.1016/j.foreco.2018.09.021.

McCabe, G. J., and Clark, M. P. (2005). Trends and Variability in Snowmelt Runoff in the Western United States. *J Hydrometeorol* 6, 476–482. doi: 10.1175/JHM428.1.

McGrath, D., Zeller, L., Bonnell, R., Reis, W., Kampf, S., Williams, K., et al. (2023). Declines in Peak Snow Water Equivalent and Elevated Snowmelt Rates Following the 2020 Cameron Peak Wildfire in Northern Colorado. *Geophys Res Lett* 50. doi: 10.1029/2022GL101294.

Moeser, C. D., Broxton, P. D., Harpold, A., and Robertson, A. (2020). Estimating the Effects of Forest Structure Changes From Wildfire on Snow Water Resources Under Varying Meteorological Conditions. *Water Resour Res* 56, 1–23. doi: 10.1029/2020WR027071.

Molotch, N. P., Brooks, P. D., Burns, S. P., Litvak, M., Monson, R. K., McConnell, J. R., et al. (2009). Ecohydrological controls on snowmelt partitioning in mixed-conifer sub-alpine forests. *Ecohydrology* 2, 129–142. doi: 10.1002/eco.48.

Molotch, N. P., Colee, M. T., Bales, R. C., and Dozier, J. (2005). Estimating the spatial distribution of snow water equivalent in an alpine basin using binary regression tree models: The impact of digital elevation data and independent variable selection. *Hydrol Process* 19, 1459–1479. doi: 10.1002/hyp.5586.

Moore, C., Kampf, S., Stone, B., and Richer, E. (2015). A GIS-based method for defining snow zones: application to the western United States. *Geocarto Int* 30, 62–81. doi: 10.1080/10106049.2014.885089.

Mote, P. W., Hamlet, A. F., Clark, M. P., and Lettenmaier, D. P. (2005). DECLINING MOUNTAIN SNOWPACK IN WESTERN NORTH AMERICA*. *Bull Am Meteorol Soc* 86, 39–50. doi: 10.1175/BAMS-86-1-39.

Mote, P. W., Li, S., Lettenmaier, D. P., Xiao, M., and Engel, R. (2018). Dramatic declines in snowpack in the western US. *NPJ Clim Atmos Sci* 1, 2. doi: 10.1038/s41612-018-0012-1.

Mueller, S. E., Thode, A. E., Margolis, E. Q., Yocom, L. L., Young, J. D., and Iniguez, J. M. (2020). Climate relationships with increasing wildfire in the southwestern US from 1984 to 2015. *For Ecol Manage* 460. doi: 10.1016/J.FORECO.2019.117861.

Murray, F. W. (1967). On the Computation of Saturation Vapor Pressure. *Journal of Applied Meteorology* 6, 203–204. doi: 10.1175/1520-0450(1967)006<0203:OTCOSV>2.0.CO;2.

Musselman, K. N., Clark, M. P., Liu, C., Ikeda, K., and Rasmussen, R. (2017). Slower snowmelt in a warmer world. *Nat Clim Chang* 7, 214–219. doi: 10.1038/nclimate3225.

Musselman, K. N., Molotch, N. P., and Brooks, P. D. (2008). Effects of vegetation on snow accumulation and ablation in a mid-latitude sub-alpine forest. *Hydrol Process* 22, 2767–2776. doi: 10.1002/HYP.7050.

O'Leary, D. S., Bloom, T. D., Smith, J. C., Zemp, C. R., and Medler, M. J. (2016). A new method comparing snowmelt timing with annual area burned. *Fire Ecology* 12, 41–51. doi: 10.4996/fireecology.1201041.

Painter, T. H., Molotch, N. P., Cassidy, M., Flanner, M., and Steffen, K. (2007). Contact spectroscopy for determination of stratigraphy of snow optical grain size. *Journal of Glaciology* 53, 121–127. doi: 10.3189/172756507781833947.

Rodman, K. C., Veblen, T. T., Chapman, T. B., Rother, M. T., Wion, A. P., and Redmond, M. D. (2020). Limitations to recovery following wildfire in dry forests of southern Colorado and northern New Mexico, USA. *Ecological Applications* 30. doi: 10.1002/eap.2001.

Roth, T. R., and Nolin, A. W. (2017). Forest impacts on snow accumulation and ablation across an elevation gradient in a temperate montane environment. *Hydrol Earth Syst Sci* 21, 5427–5442. doi: 10.5194/HESS-21-5427-2017.

Rother, M. T., and Veblen, T. T. (2016). Limited conifer regeneration following wildfires in dry ponderosa pine forests of the Colorado Front Range. *Ecosphere* 7. doi: 10.1002/ecs2.1594.

Rouse, W. R. (1984). Microclimate at Arctic Tree Line 1. Radiation Balance of Tundra and Forest. *Water Resour Res* 20, 57–66. doi: 10.1029/WR020i001p00057.

Shi, K., and Touge, Y. (2023). Identifying the shift in global wildfire weather conditions over the past four decades: an analysis based on change-points and long-term trends. 10, 3. doi: 10.1186/s40562-022-00255-6.

884 Smoot, E. E., and Gleason, K. E. (2021). Forest Fires Reduce Snow-Water Storage and Advance
885 the Timing of Snowmelt across the Western U.S. *Water (Basel)* 13, 3533. doi:
886 10.3390/w13243533.
887 Stevens-Rumann, C. S., and Morgan, P. (2019). Tree regeneration following wildfires in the
888 western US: a review. *Fire Ecology* 15. doi: 10.1186/s42408-019-0032-1.
889 Sturm, M., Goldstein, M. A., and Parr, C. (2017). Water and life from snow: A trillion dollar
890 science question. *Water Resour Res* 53, 3534–3544. doi: 10.1002/2017WR020840.
891 Troendle, C. A., and King, R. M. (1985). The Effect of Timber Harvest on the Fool Creek
892 Watershed, 30 Years Later. *Water Resour Res* 21, 1915–1922. doi:
893 10.1029/WR021i012p01915.
894 Trujillo, E., Ramírez, J. A., and Elder, K. J. (2007). Topographic, meteorologic, and canopy
895 controls on the scaling characteristics of the spatial distribution of snow depth fields. *Water*
896 *Resour Res* 43. doi: 10.1029/2006WR005317.
897 Trujillo, E., Ramírez, J. A., and Elder, K. J. (2009). Scaling properties and spatial organization of
898 snow depth fields in sub-alpine forest and alpine tundra. *Hydrol Process* 23, 1575–1590.
899 doi: 10.1002/hyp.7270.
900 Uecker, T. M., Kaspari, S. D., Musselman, K. N., and Skiles, S. M. (2020). The post-wildfire
901 impact of burn severity and age on black carbon snow deposition and implications for snow
902 water resources, cascade range, Washington. *J Hydrometeorol* 21, 1777–1792. doi:
903 10.1175/JHM-D-20-0010.1.
904 Viviroli, D., Dürr, H. H., Messerli, B., Meybeck, M., and Weingartner, R. (2007). Mountains of
905 the world, water towers for humanity: Typology, mapping, and global significance. *Water*
906 *Resour Res* 43. doi: 10.1029/2006WR005653.
907 Wagner, A. M., Bennett, K. E., Liston, G. E., Hiemstra, C. A., and Cooley, D. (2021). Multiple
908 indicators of extreme changes in snow-dominated streamflow regimes, Yakima river basin
909 region, USA. *Water (Switzerland)* 13. doi: 10.3390/w13192608.
910 Webb, R., Litvak, M., and Brooks, P. D. (2023). The role of terrain-mediated hydroclimate in
911 vegetation recovery after wildfire. *Environmental Research Letters*. doi: 10.1088/1748-
912 9326/acd803.
913 Westerling, A. L. (2016). Increasing western US forest wildfire activity: sensitivity to changes in
914 the timing of spring. *Philosophical Transactions of the Royal Society B: Biological*
915 *Sciences* 371, 20150178. doi: 10.1098/rstb.2015.0178.
916 Westerling, A. L., Hidalgo, H. G., Cayan, D. R., and Swetnam, T. W. (2006). Warming and
917 Earlier Spring Increase Western U.S. Forest Wildfire Activity. *Science (1979)* 313, 940–
918 943. doi: 10.1126/science.1128834.
919 Westerling, A. L., Turner, M. G., Smithwick, E. A. H., Romme, W. H., and Ryan, M. G. (2011).
920 Continued warming could transform greater yellowstone fire regimes by mid-21st century.
921 *Proc Natl Acad Sci U S A* 108, 13165–13170. doi: 10.1073/pnas.1110199108.
922 Williams, L. D., Barry, R. G., and Andrews, J. T. (1972). Application of computed global
923 radiation for areas of high relief. *Journal of Applied Meteorology* 11, 526–533. doi:
924 10.1175/1520-04501972011<0526:aocgrf<2.0.co;2.
925 Wrzesien, M. L., Durand, M. T., Pavelsky, T. M., Kapnick, S. B., Zhang, Y., Guo, J., et al.
926 (2018). A New Estimate of North American Mountain Snow Accumulation From Regional
927 Climate Model Simulations. *Geophys Res Lett* 45, 1423–1432. doi:
928 10.1002/2017GL076664.